

Preparatory acoustic emission activity of hydraulic fracture in granite with various viscous fluids revealed by deep learning technique

Rui Tanaka,¹ Makoto Naoi²,^{ORCID} Youqing Chen,³ Kazune Yamamoto,¹ Keiichi Imakita,¹ Naofumi Tsutsumi,³ Akihiro Shimoda,¹ Daiki Hiramatsu,³ Hironori Kawakata,⁴ Tsuyoshi Ishida,¹ Eiichi Fukuyama,¹ Hiroyuki Tanaka,⁵ Yutaro Arima,⁵ Shigehiro Kitamura⁵ and Daisuke Hyodo⁵

¹Department of Civil and Earth Resources Engineering, Graduate School of Engineering, Kyoto University, Kyoto Daigaku Katsura Cluster-C, Nishikyo-ku, Kyoto 615–8540, Japan

²Research Center for Earthquake Prediction, Disaster Prevention Research Institute, Kyoto University, Gokasyo, Uji, Kyoto 611-0011, Japan. E-mail: naoi.makoto.4z@kyoto-u.ac.jp

³Department of Energy Science and Technology, Graduate School of Energy Science, Kyoto University, Yoshida-Honmachi, Sakyo-ku, Kyoto 606–8501, Japan

⁴College of Science and Engineering, Ritsumeikan University, 1-1-1 Noji Higashi, Kusatsu, Shiga 525–8577, Japan

⁵Japan Oil, Gas and Metals National Corporation, 1-2-2 Hamada, Mihama-ku, Chiba 261-0025, Japan

Accepted 2021 March 5. Received 2021 February 22; in original form 2020 August 13

SUMMARY

To investigate the influence of fluid viscosity on the fracturing process, we conducted hydraulic fracturing experiments on Kurokami-jima granite specimens with resins of various viscosities. We monitored the acoustic emission (AE) activity during fracturing and estimated the moment tensor (MT) solutions for 54 727 AE events using a deep learning technique. We observed the breakdown at 14–22 MPa of borehole pressure, which was dependent on the viscosity, as well as two preparatory phases accompanying the expansion of AE-active regions. The first expansion phase typically began at 10–30 per cent of the breakdown pressure, where AEs occurred three-dimensionally surrounding the wellbore and their active region expanded with time towards the external boundaries of the specimen. The MT solutions of these AEs corresponded to crack-opening (tensile) events in various orientations. The second expansion phase began at 90–99 per cent of the breakdown pressure. During this phase, a new planar AE distribution emerged from the borehole and expanded along the maximum compression axis, and the focal mechanisms of these AEs corresponded to the tensile events on the AE-delineating plane. We interpreted that the first phase was induced by fluid penetration into pre-existing microcracks, such as grain boundaries, and the second phase corresponded to the main fracture formation. Significant dependences on fluid viscosity were observed in the borehole pressure at the time of main fracture initiation and in the speed of the fracture propagation in the second phase. The AE activity observed in the present study was fairly complex compared to that observed in previous experiments conducted on tight shale samples. This difference indicates the importance of the interaction between the fracturing fluid and pre-existing microcracks in the fracturing process.

Key words: Fracture and flow; Earthquake source observations; Induced seismicity; Fractures, faults, and high strain deformation zones.

1 INTRODUCTION

In the development of unconventional resources, such as shale gas/oil production and enhanced geothermal system, hydraulic fracturing is used to increase the permeability of tight rock mass for resource extraction. Many previous studies have shown that fracturing processes depend on the viscosity of the fracturing fluid.

For example, Zhang *et al.* (2016) conducted numerical simulations using the discrete element method and showed that wide fractures were induced with a fracturing fluid of high viscosity. A wide fracture efficiently accommodates proppants (fine particles of sand or ceramic designed to support induced fractures), which is advantageous to maintaining high permeability (e.g. Maxwell & Cipolla 2011). Warpinski *et al.* (2005) performed hydraulic fracturing for

gas extraction in the Barnett shale formation in Texas, USA, at a depth of ~ 2.3 km using low-viscosity fluid (slickwater) and high-viscosity gel. They reported that the stimulated reservoir volume (Mayerhofer *et al.* 2010) was greater, and the gas production rates were higher in the case of slickwater.

In addition, the influence of viscosity of the fracturing fluid on hydraulic fracturing has been studied through laboratory experiments. For example, it has been repeatedly reported that breakdown (a steep drop in fluid pressure associated with macroscopic fracture formation) occurs at high fluid pressure with high viscosity fluid (Ishida *et al.* 2016; Fallahzadeh *et al.* 2017). Stanchits *et al.* (2015) conducted hydraulic fracturing experiments on Colton sandstone and Niobrara shale in a laboratory and showed that the fracture width and number of acoustic emission (AE) events during the experiments increased with the viscosity of the fracturing fluid. Ishida *et al.* (2016) analysed the P -wave first-motion polarities of AE events induced by hydraulic fracturing on Kurokami-jima granite in a laboratory and showed that AE events corresponding to a crack opening (i.e. tensile events) became dominant with higher-viscosity fluid. They also observed the induced fractures on thin-section slices and pointed out that more complex fractures were induced with a low-viscosity fluid.

In this study, we investigated the influence of fracturing fluid viscosity on hydraulic fracturing under uniaxial loading conditions in laboratory experiments. The fracturing processes were examined through AE measurement and direct observation of fluid penetration regions, which was enabled using a fluorescent resin as the fracturing fluid. This experimental approach was used in our previous studies, allowing us to observe the temporal development and detailed structure of the induced fractures. For example, Naoi *et al.* (2018) and Yamamoto *et al.* (2019) demonstrated that AE activity, fluid pressure history, and dominant fracture modes strongly depend on the orientation of pre-existing microcracks in a specimen. Naoi *et al.* (2020) illustrated that simple bi-wing tensile fractures were induced in experiments conducted on a very tight shale, consistent with the classical theory of hydraulic fracturing (e.g. Hubbert & Willis 1957). Chen *et al.* (2018) focussed on the morphology of hydraulically induced fractures in shale samples and showed that the pre-existing fractures strongly influenced the complexity of the induced fractures.

In the present experiments, we used Kurokami-jima granite specimens from Yamaguchi Prefecture, Japan, for which a significant interaction between pre-existing microcracks (such as grain boundaries) and fracturing fluid was observed in the experiments conducted by Naoi *et al.* (2018) and Yamamoto *et al.* (2019). To investigate the viscosity dependence of the fracturing process, we used fluorescent resins of five different viscosities as the fracturing fluid, which were adjusted using a thickener, and the fluid penetration regions were observed after fracturing. In addition, we monitored the AEs and investigated their fracture modes by moment tensor (MT) analysis. MT analysis of AEs in laboratory experiments requires careful sensitivity calibration of AE transducers (e.g. Aker *et al.* 2014; Kwiatek *et al.* 2014). Thus, we conducted a pulse radiation test for calibration (Yamamoto *et al.* 2019; Naoi *et al.* 2020) immediately before each fracturing experiment. We also estimated the anisotropic attenuation of each specimen using the test data and corrected the effect in the MT analysis because the orthorhombic anisotropy of granite (e.g. Nara & Kaneko 2006) can cause negative bias in MT estimates, especially in tensile-type events (Stierle *et al.* 2016), which are expected to be induced by hydraulic fracturing. Meanwhile, we introduced a convolutional neural network (CNN; e.g. LeCun *et al.* 1998) technique to estimate many MT solutions,

and we then observed the details of temporal changes in the focal mechanisms.

2 EXPERIMENTAL METHOD

2.1 Sample and experimental procedure

We used 10 Kurokami-jima granite specimens (Table 1), each with dimensions of $65 \times 65 \times 130$ mm³. Granite generally has a rift plane in which the rock splits most easily, reflecting the lowest tensile strength, and its P -wave velocity orthogonal to the plane is the lowest (Sano *et al.* 1992). Kurokami-jima granite also exhibits these features (Kudo *et al.* 1986, 1987). In this study, we prepared a block of dimensions $280 \times 280 \times 280$ mm³ and estimated the direction of the rift plane from its P -wave anisotropy. From this block, we extracted $65 \times 65 \times 130$ mm³ specimens whose rift planes were orthogonal to the longitudinal direction. Elastic wave velocities along the x -, y -, and z -directions (Fig. 1) were measured for each specimen (Table 1). The obtained values were ~ 5 km s⁻¹ or more, indicating that these specimens remained intact without substantial defects.

Fig. 2 shows the polarizing microscopy observation of a thin section extracted from the block. We observed an equigranular texture composed of quartz, plagioclase and potassium feldspar, which had a dominant grain size of ~ 0.9 mm. Coarser quartzes and plagioclase crystals of 3–4 mm in size were occasionally identified. The boundaries of such grains are expected to act as minor defects or weak planes in hydraulic fracturing (Chen *et al.* 2015).

We conducted hydraulic fracturing on air-dried specimens at a uniaxial loading of 5 MPa (Fig. 1) in a laboratory under the same setting as that used by Naoi *et al.* (2020). We set a packer in a 6-mm-diameter borehole, which was drilled in the centre of the specimen, to create a 30-mm pressurized section (within $x = \pm 15$ mm) by using a couple of O-rings. A thermosetting acrylic resin, or methyl methacrylate (MMA, with ~ 0.8 mPa s viscosity at room temperature and pressure), was injected into the section by a cylindrical piston, which was pressurized by water injection from a syringe pump at a constant flow rate of 1 cc min⁻¹ (1.67×10^{-8} m³ s⁻¹). Details of the injection system are described in Akai *et al.* (2015). In addition to the MMA of ~ 0.8 mPa s viscosity, we prepared MMAs of various other viscosities by adding a little Sumecton-STN (Kunimine Industries Co., Ltd.), a thickener derived from hectorite. Their viscosities were adjusted to ~ 10 , ~ 50 , ~ 300 and ~ 1000 mPa s, each of which were used to fracture two specimens. The actual viscosities of the fracturing fluids were measured immediately before each experiment (Table 1).

The fluid pressure applied to the pressurized section of the borehole (hereinafter ‘borehole pressure’) was measured using a pressure gauge placed ~ 700 mm from the packer. The gauge was connected to the packer via a stainless-steel pipe of 1 mm inner diameter. The pressure loss between the gauge and packer was expected to be proportional to the fluid viscosity and was estimated to be ~ 0.5 MPa at maximum (under the assumption of a viscosity of 1000 mPa s and an injection rate of 1 cc min⁻¹). This value of pressure loss does not affect any of the discussions conducted in the present paper.

The use of a fracturing fluid containing a fluorescent compound allowed us to observe the fluid penetration regions. Immediately after each experiment, we heated the fractured specimen in a furnace at a minimum temperature of 80 °C for at least 12 h to solidify the penetrating fluid. We then cut the specimen into five cross-sectional slices parallel to the y - z planes at $x = -21.7$, -10.8 , 0 , $+10.8$, and

Table 1. Experimental results, elastic wave velocities and quality factors of each specimen.

Sample	Viscosity of fracturing fluid (mPa s)	No. of well-located AE events	No. of DD-relocated AE events	P^{init} (MPa)	t^{init} (s)	P^{BD} (MPa)	V_P^x (km s ⁻¹)	V_P^y (km s ⁻¹)	V_P^z (km s ⁻¹)	V_S^x (km s ⁻¹)	V_S^y (km s ⁻¹)	V_S^z (km s ⁻¹)	Q^x	Q^y	Q^z
KJG1810	0.69	6057	6013	13.35	1434.15	14.61	5.29	5.29	4.96	3.09	3.08	3.03	21.56	26.10	13.35
KJG1811	0.63	3864	3848	13.54	671.50	14.10	5.22	5.24	4.88	3.09	3.10	3.04	20.00	21.57	12.65
KJG1813	10.5	3755	3739	15.12	1053.20	15.31	5.27	5.37	5.00	2.94	2.97	2.96	18.14	30.90	10.15
KJG1816	11.6	4023	4033	16.65	1483.65	16.79	5.30	5.24	4.92	3.14	3.08	3.05	17.06	19.78	12.17
KJG1802	57.2	8170	8139	20.08	801.20	20.28	5.31	5.25	4.97	3.07	3.10	3.03	18.26	18.05	11.87
KJG1805	46.7	8216	8163	18.44	652.25	18.62	5.25	5.30	5.02	3.07	3.20	3.06	16.28	16.79	10.90
KJG1804	341	10 050	10 010	22.18	737.90	22.30	5.28	5.26	4.95	3.15	3.11	3.13	19.20	23.54	13.13
KJG1809	329	6295	6272	21.87	686.70	21.93	5.28	5.29	5.00	3.09	3.15	3.11	22.94	27.67	15.71
KJG1803	1010	12 872	12 830	21.81	512.00	21.92	5.34	5.37	5.09	3.17	3.14	3.15	18.37	20.75	12.82
KJG1806	1090	10 106	10 079	20.85	589.05	20.94	5.38	5.38	5.10	3.11	3.15	3.01	16.66	9.71	11.26

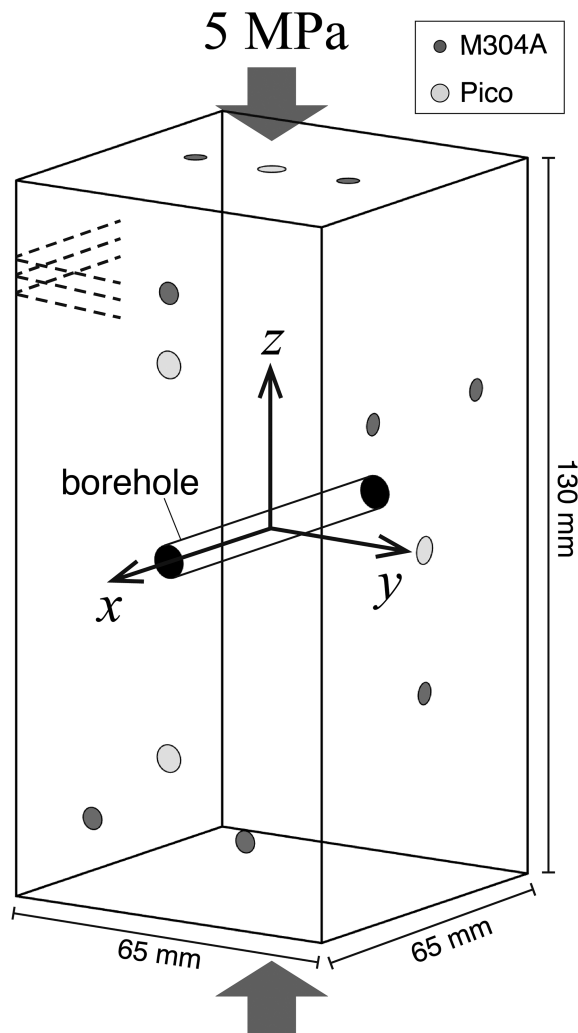


Figure 1. Schematic view of a specimen, the AE sensor layout and the coordinate system. The dashed lines indicate the rift plane direction.

+21.7 mm, and took their photographs with UV light irradiation under identical photographing conditions.

2.2 AE measurement and cataloguing procedure

We measured the AE events induced by fracturing and developed their catalogue using the method of Naoi *et al.* (2020). As shown in Fig. 1, we attached 16 high-sensitivity broad-band transducers (M304A, Fuji Ceramics Corp., 4 mm in diameter) and 8 transducers with a resonance frequency of ~ 550 kHz (PICO: Physical Acoustics Co., 5 mm in diameter) onto a specimen. M304A exhibits high sensitivity and a broad frequency range owing to its built-in preamplifier. Although PICO exhibits lower receiver performance, it can radiate an acoustic wave; this function is necessary in pulse radiation tests (Section 4.1). The transducers on the side faces of a specimen were attached using thermofusible wax, and the ones on the top and bottom were placed with springs in small holes drilled into each stainless-steel loading plate. The waveforms received at M304A were recorded only after 45 dB amplification, and those of PICO were recorded after the application of 46 dB amplification and a 0.02–3.00 MHz bandpass filter. All waveform data were continuously recorded at 10 MS s^{-1} using a 14-bit analogue-to-digital converter (PXI-5170R, National Instruments Co.).

From the obtained continuous data for each experiment, we extracted 2048 sample waveforms around AE events that were detected using a ratio of short- and long-term average (Allen 1978). We automatically read the P -wave arrival times of the cut-out waveforms using Takanami & Kitagawa's (1988) algorithm and estimated their hypocentres, origin times and standard errors by using a least-squares method considering P -wave anisotropy (Rothman *et al.* 1974). We selected well-located events satisfying the following two criteria: (1) the maximum of the three standard errors along each principal axis of an error ellipsoid was less than 10 mm and (2) the number of P -wave arrival times used in the hypocentre location exceeded 8 (Naoi *et al.* 2018). We then relocated the hypocentres using the double-difference (DD) method (Waldhauser & Ellsworth 2000), with the arrival time differences calculated from the automatically picked arrival times and those evaluated using a cross-correlation method. In the following analyses, we used the hypocentres determined by the DD method.

We estimated the relative magnitude M of each event using the equation

$$M = \sum \log_{10} (r_i \times A_i) / N \quad (1)$$

where A_i is the peak-to-peak amplitude (mV) of the cut-out waveform recorded at the i th transducer, r_i is the distance between transducer i and the hypocentre (mm) and N is the number of transducers used in the calculation (Naoi *et al.* 2018). The influence of anelastic attenuation is not considered here. We only used waveforms whose signal-to-noise ratio (SNR) was three or more.

3 FLUID PRESSURE HISTORY, AE ACTIVITY AND FLUID PENETRATION REGIONS DEPENDING ON VISCOSITY OF FRACTURING FLUID

3.1 Example of experiments conducted with low-viscosity fluid (KJG1811; viscosity $\sim 0.8 \text{ mPa s}$)

As an example of the experiments conducted using MMA without a thickener, the changes in borehole pressure, cumulative number of AEs, z -coordinates of AE hypocentres, and relative magnitudes in the experiment conducted on KJG1811 are shown in Figs 3(a)–(c), and their enlarged views around the breakdown are shown in Figs 3(d)–(f). The horizontal axes show the elapsed time, which takes the timing of the borehole pressure peak as the origin. As shown in Fig. 3(a), the borehole pressure gradually increased with time. Its rate of increase became constant at $t \sim -270$ s and started to decrease at $t \sim -20$ s (Fig. 3d). Then, the pressure attained the peak value of 14.1 MPa (breakdown pressure; P^{BD}) at $t = 0$ s (breakdown time; t^{BD}), followed by a rapid drop in the borehole pressure due to the generation of a macroscopic failure (breakdown). At this time, the fluid leaked from the induced fractures appearing on the two surfaces perpendicular to the x -axis of the specimen. Similar leaks from surface fractures were observed in all experiments. After the breakdown, the borehole pressure became stable at ~ 7 MPa (at $t \sim 100$ s) and decreased when the fluid injection stopped at $t \sim 120$ s. At $t \sim 245$ s, we opened a valve in the injection system to completely release the borehole pressure.

The cumulative number of AEs increased with borehole pressure. A significant increase in the AE occurrence rate (dashed black lines in Figs 3a–c indicate the timing when the rate exceeded four events per second) was initiated simultaneously with the initiation of the linear increase in the borehole pressure. From this point onward,

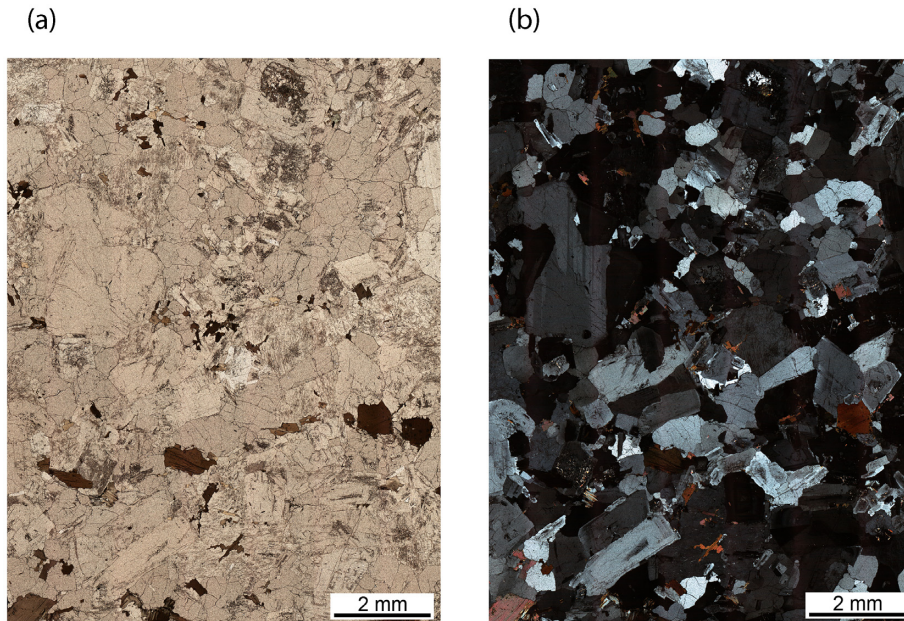


Figure 2. Photomicrograph of Kurokami-jima granite taken under (a) plane polarized light and (b) crossed Nicols.

the AE-active regions gradually expanded outward from the pressurized section of the borehole ($z = 0$ mm; Fig. 3b). We refer to this expansion phase of the AE activity as the ‘first expansion phase’. In addition, the AE occurrence rate started to increase markedly at $t \sim -20$ s (solid black lines in Figs 3a–f), which occurred simultaneously with the initiation of the deviation of the borehole pressure from the linearly increasing trend. These AEs corresponded to a planar distribution along the x – z plane that emerged around the pressurized section of the borehole and expanded in the z -direction (Figs 3b and e). We refer to this expansion phase as the ‘second expansion phase’. Stanchits *et al.* (2014), based on the experimental results obtained on Colton sandstone, indicated that the timing at which the borehole pressure started to deviate from the linearly increasing trend corresponded to the initiation of a dry hydraulic fracture. In the present study, as discussed later, we also obtained evidence that a main hydraulic fracture was initiated at that time. A borehole pressure at this timing was called ‘leak-off pressure’ in our previous study (Naoi *et al.* 2018), while we refer here to it as the ‘fracture initiation pressure’ (P^{init}) and its timing as the ‘fracture initiation time’ (t^{init}). After t^{init} , the AE occurrence rate decreased rapidly, and slightly increased when the fluid injection stopped (at $t \sim 120$ s) and the borehole pressure was released (at $t \sim 245$ s). The averages of the relative magnitudes began to increase at t^{init} and reached a maximum immediately after t^{BD} , and then decreased.

Fig. 4 shows a photograph of the cross-sectional slice of KJG1811 at $x = 0$, taken under UV light irradiation, where the bright and bluish-white parts correspond to the fluid penetration regions, including induced fractures. A higher luminance indicates the penetration of more fracturing fluid. AE hypocentres before t^{init} (Fig. 4a), from t^{init} to t^{BD} (Fig. 4b), and after t^{BD} (Fig. 4c) are overlaid on the photograph. Before t^{init} , the AEs were widely distributed in the fluid penetration region (Fig. 4a). In addition to this distribution, an AE alignment along the z -direction emerged in the second expansion phase (Fig. 4b). After t^{BD} , the alignment extended further from the borehole (Fig. 4c).

Based on these features, we interpreted that the first expansion phase was caused by the penetration of the fracturing fluid into pores and pre-existing microcracks. We also interpreted that the second expansion phase corresponded to the quasi-static propagation of a main hydraulic fracture along the z -direction. According to the classical theory of hydraulic fracturing based on the solution of a stress field around a borehole (Hubbert & Willis 1957), hydraulic fractures are expected to propagate in the direction of maximum compression. The AE alignment observed in the second expansion phase was consistent with this expectation. The breakdown, or the rapid drop in borehole pressure, is likely to have occurred because of the dynamic propagation, as a result of the fracture growth exceeding the critical crack size. Similar AE activity, likely to be representing a transition from quasi-static to dynamic propagation, was observed in previous experiments conducted on Eagle Ford shale (Naoi *et al.* 2020). AEs that still occurred after the breakdown (Fig. 3b), were likely to be due to the stress disturbance caused by the induced fractures and the penetration of fracturing fluid into these fractures, including the subsidiary ones (Yamamoto *et al.* 2019).

3.2 Example of experiments conducted with high-viscosity fluid (KJG1804; viscosity ~ 300 mPa s)

As an example of the experiments conducted with a higher-viscosity fluid, the experimental results obtained for KJG1804 (fracturing fluid viscosity ~ 300 mPa s) are shown in Fig. 5. Features similar to those observed for KJG1811 (fracturing fluid viscosity ~ 0.8 mPa s; Fig. 3) were observed in the temporal changes in the cumulative number of AEs, AE-active regions, and relative magnitudes. Meanwhile, the second expansion phase started only 3.3 s before t^{BD} , which was significantly later than ~ 20 s for KJG1811, and the duration of the second expansion phase was significantly shorter for KJG1804 than that for KJG1811. Such shorter second expansion phases were observed for all experiments with fracturing fluids of more than ~ 10 mPa s viscosity.

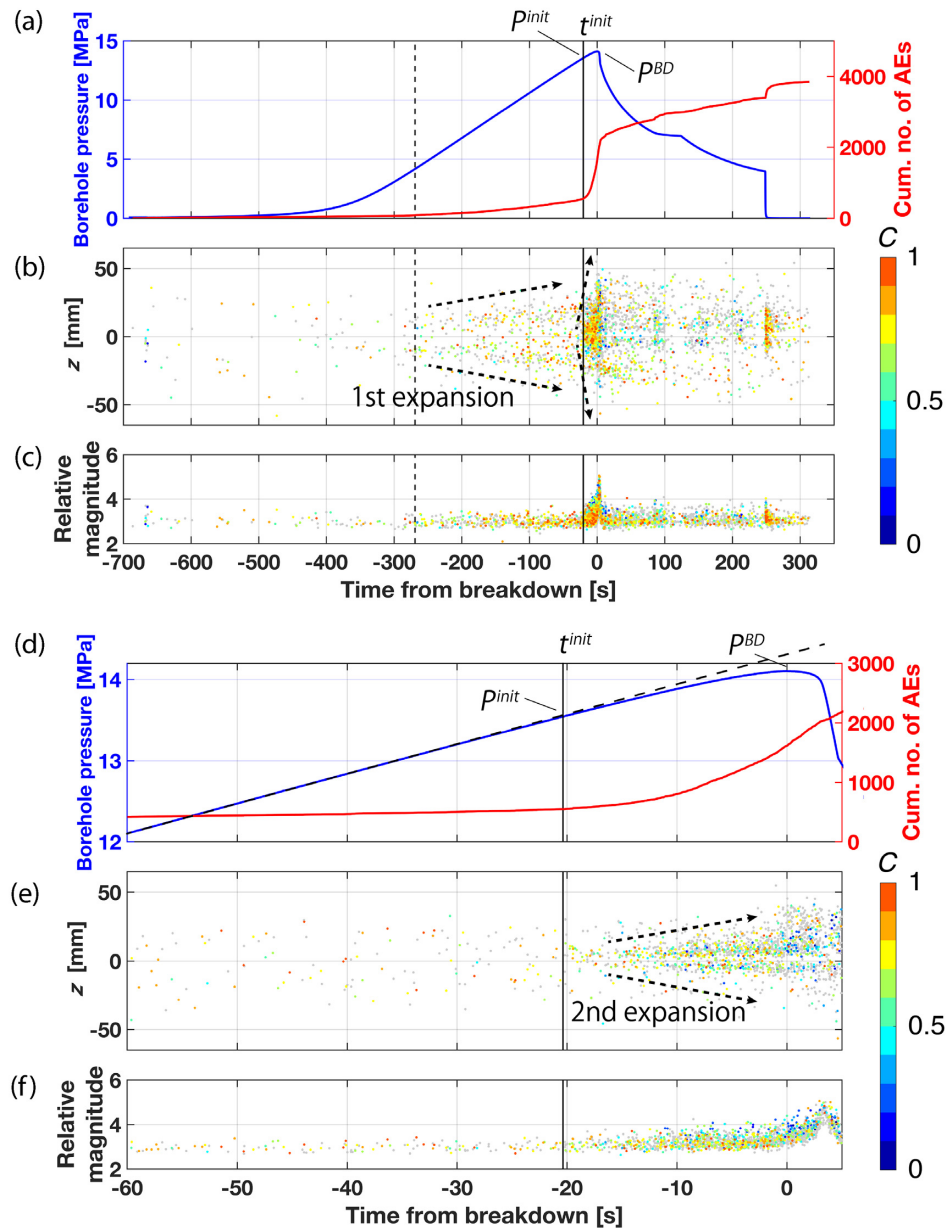


Figure 3. Borehole pressure history and AE activity against relative time whose origin corresponds to t^{BD} in the experiment conducted on KJG1811 (fracturing fluid viscosity ~ 0.8 mPa s). (a) Temporal changes in borehole pressure and the cumulative number of AEs. (b) Change in the z -coordinates of the hypocentres. (c) Change in the relative magnitudes. (d–f) Enlarged views of (a)–(c) around t^{BD} . The dots in (b), (c), (e), and (f) are colour-coded according to the c -values of MT solutions for tensile-dominated or DC-dominated events. The vertical dashed black lines in (a)–(c) indicate the time at which the AE occurrence rate exceeds four events s^{-1} . The solid black lines indicate the timing of the fracture initiation (t^{init}).

3.3 Influence of viscosity of fracturing fluid

Fig. 6 shows the relations of p^{BD} , p^{init} , $p^{BD} - p^{init}$ and $t^{BD} - t^{init}$ with the viscosity of the fracturing fluid for each experiment. Higher p^{BD} and p^{init} values were observed in the experiments conducted with higher viscosity (Fig. 6a). The use of a higher-viscosity fluid resulted in a smaller change in borehole pressure during the second expansion phase (Fig. 6b), as well as its shorter duration (Fig. 6c); that is, the quasi-static fracture was likely to have grown faster and reached the critical size rapidly.

Fig. 7 shows photographs of the cross-sectional slices at $x = 0$ mm for five specimens that were fractured by a fluid of ~ 0.8 , ~ 10 , ~ 50 , ~ 300 and ~ 1000 mPa s viscosities. In all specimens, an

elliptical fluid penetration region of 20–30 mm width was observed around the borehole. This region was smaller for specimens with higher-viscosity fluids, indicating that the penetration of a higher-viscosity fluid into the rock matrix is more difficult. In all specimens, the AE events during the first expansion phase spread out over the region. In addition, in all specimens fractured with fluids of 10 mPa s or more viscosity, a thin, high-luminescence elongated region from the borehole along the z -axis could be recognized. A 2-D AE distribution delineating the region appeared after t^{init} , which was likely to be corresponding to the formation of a main hydraulic fracture. Even in the experiments conducted with a fluid of ~ 0.8 mPa s viscosity (KJG1810 and KJG1811), such planar

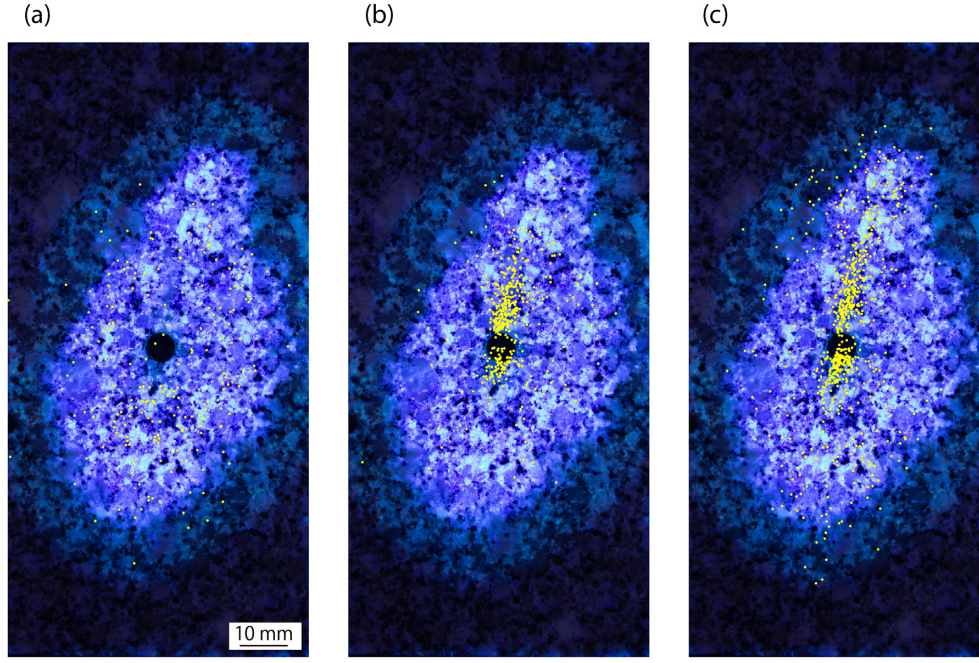


Figure 4. Fluid penetration region revealed by the fluorescence method on KJG1811 (~ 0.8 MPa s) on the y - z plane at $x = 0$. The black circles in the centre correspond to the borehole. The DD-relocated hypocentres, within $x = \pm 5$ mm (yellow dots), are overlaid for AEs (a) before t^{init} , (b) from t^{init} to t^{BD} and (c) after t^{BD} .

AE distribution was recognized, although the corresponding high-luminescence region was not observed (Figs 4 and 7a and f).

4 MOMENT TENSOR ANALYSIS

4.1 Estimation of AE sensor coupling and anelastic attenuation

We estimated the MT solutions of the DD-relocated AEs from their P -wave first motion polarities and amplitudes using a method similar to that used by Yamamoto *et al.* (2019) and Naoi *et al.* (2020). The sensitivity of an AE transducer depends on its coupling condition; that is, the obtained amplitudes are influenced by the coupling condition. To correct this influence, we conducted a pulse radiation test in which a pulse radiated from each PICO was received at the other 23 transducers before each fracturing experiment. Based on the obtained P -wave first motion amplitudes, we inversely estimated the coupling condition of each transducer. In addition, the parameter of anelastic attenuation (quality factor Q) was estimated from the same data under the assumption of an orthorhombic anisotropy in the x -, y -, and z -directions. The approach was the same as that used by Naoi *et al.* (2020), except that Q was included as an unknown parameter.

When a pulse of amplitude A_0 is radiated from transmitter j , the amplitude A_{ij} obtained at receiver i can be expressed as

$$A_{ij} = S_i I_i G_{ij} I_j S_j A_0 \quad (2)$$

(summation is not taken for i and j) in the frequency domain (Kwiatek *et al.* 2014), where S_i and S_j indicate the coupling coefficients of the receiver and transmitter, respectively, G_{ij} indicates a Green's function of the medium, I_i and I_j indicate the transducer responses, including directivity, which are assumed to be bell-shaped curves defined by

$$I_i \propto \exp(-\alpha a^b), \quad I_j \propto \exp(-\alpha \beta^b). \quad (3)$$

Here, α and β are the incident and projection angles, respectively, and a and b indicate the transducer coefficients that determine the shape of the functions. In the following analyses, we used the values of $a = 0.90$, $b = 1.47$ for M304A, and $a = 0.53$, $b = 2.35$ for PICO (Naoi *et al.* 2020). As Green's function in eq. (2), we used

$$G_{ij} = \frac{1}{R_{ij}} \exp\left(\frac{\pi R_{ij} f}{V_p Q}\right), \quad (4)$$

where geometrical spreading and anelastic attenuation were considered. Here, f is the frequency, and R_{ij} is the distance between the receiver i and transmitter j . The P -wave velocity V_p and quality factor Q for a ray path are assumed to be

$$V_p = \sqrt{V_p^x l_x^2 + V_p^y l_y^2 + V_p^z l_z^2}, \quad (5)$$

$$Q = \sqrt{Q_x^2 l_x^2 + Q_y^2 l_y^2 + Q_z^2 l_z^2}, \quad (6)$$

under the assumption of an orthorhombic anisotropy, where V_p^x , V_p^y and V_p^z indicate the P -wave velocities in the x -, y - and z -directions, respectively; Q_x , Q_y , and Q_z are the quality factors in each direction; l_x , l_y and l_z are the direction cosines of a vector from transmitter j to receiver i . Based on these equations, we inversely estimated S_i , S_j , Q_x , Q_y and Q_z from the amplitudes of P -wave first motions obtained in the pulse radiation test for each fracturing experiment. As the P -wave velocities, we used the values listed in Table 1. We solved eq. (2) ignoring its frequency dependence and using $f = 265$ kHz for all data, which corresponded to the median of the pulse widths of the P -wave first motions in the pulse radiation tests (Fig. 8a). The obtained estimates of Q_x , Q_y and Q_z for each specimen are shown in Table 1.

Fig. 9(a) illustrates an example of the P -wave first motion amplitudes obtained in the pulse radiation tests (on KJG1810), and Fig. 9(b) shows the amplitudes obtained after correcting the effects of coupling and attenuation. In Fig. 9(b), the red curves, which

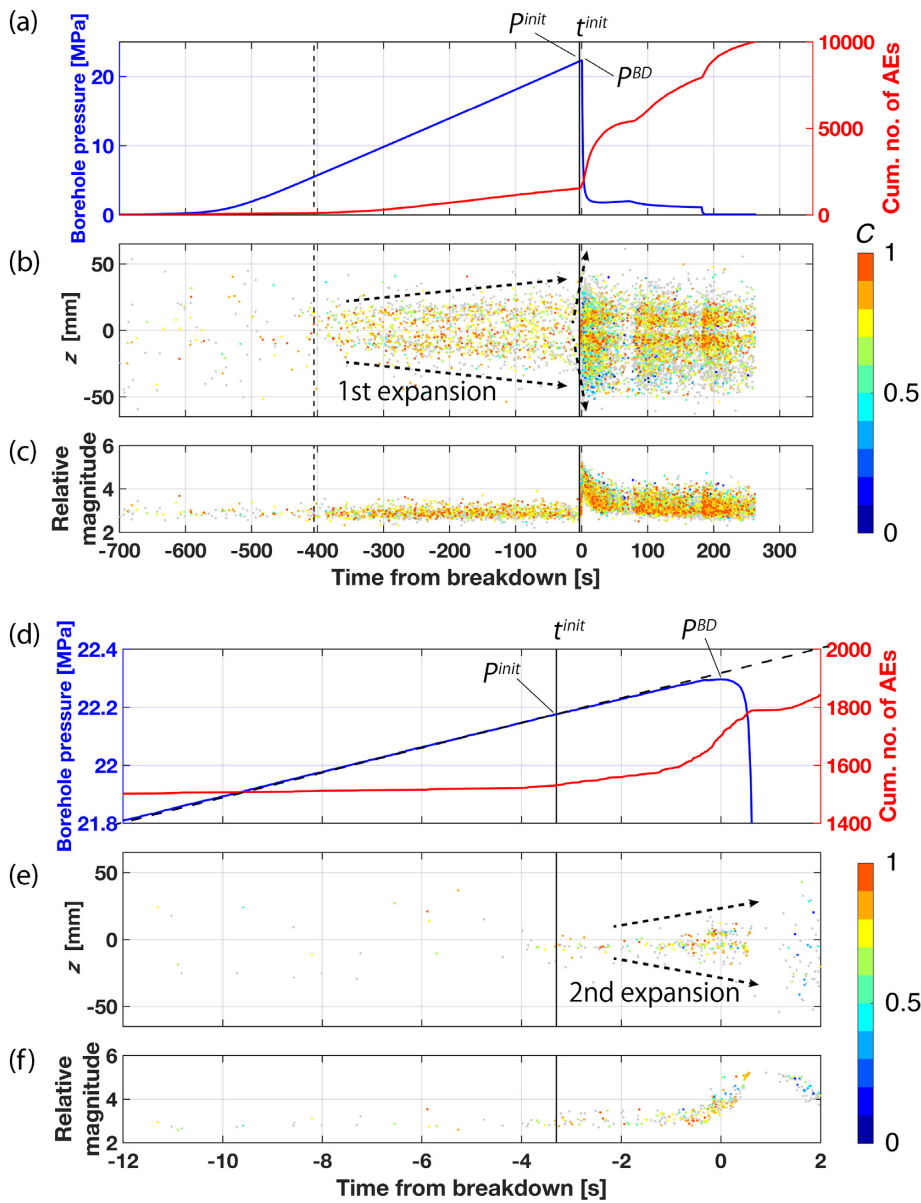


Figure 5. Borehole pressure history and AE activity in the experiment conducted on KJG1804 (~300 mPa s) in the same manner as that shown in Fig. 3.

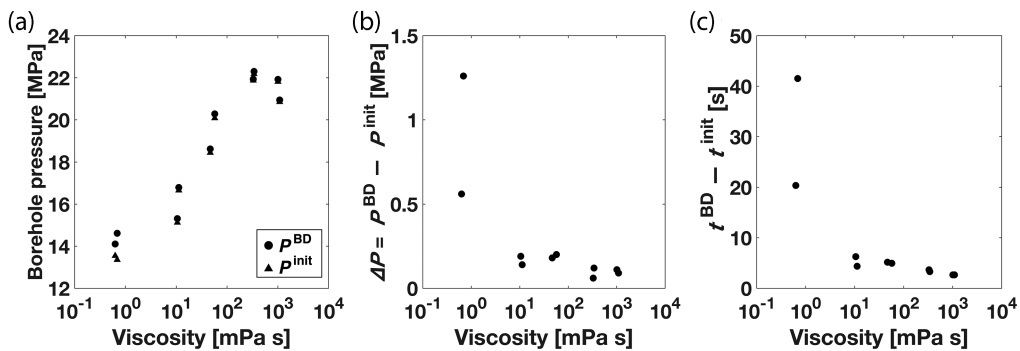


Figure 6. Relationship of fracturing fluid viscosity with (a) p^{BD} and p^{init} , (b) $\Delta P = p^{BD} - p^{init}$ and (c) $t^{BD} - t^{init}$.

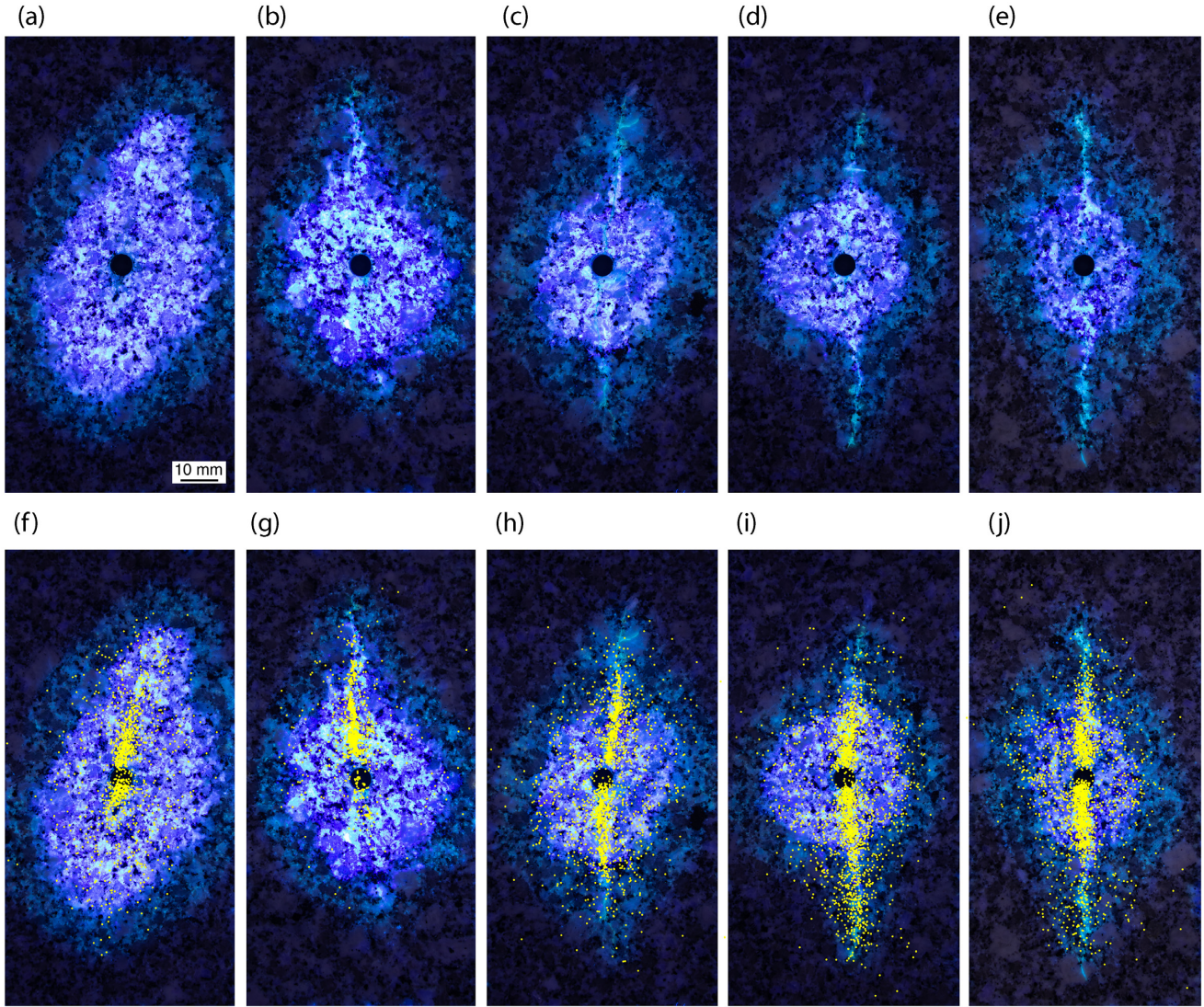


Figure 7. (a–e) Fluid penetration regions revealed by the fluorescence method on the y - z planes at $x = 0$. (f–j) The same figures with the DD-relocated hypocentres within $x = \pm 5$ mm. (a and f) KJG1811 (~ 0.8 mPa s). (b and g) KJG1813 (~ 10 mPa s). (c and h) KJG1805 (~ 50 mPa s). (d and i) KJG1804 (~ 300 mPa s). (e and j) KJG1806 (~ 1000 mPa s). As all the photographs were taken under the same conditions, we can compare the luminance among the different specimens.

represent the theoretical amplitudes for three specific cases, are overlaid, where each curve corresponds to the cases of (1) $\alpha = 0^\circ$ and $\beta = 2\theta$, (2) $\alpha = \beta = \theta$ and (3) $\alpha = 2\theta$ and $\beta = 0^\circ$ when M304A receives a pulse wave radiated from PICO. Case (1) also corresponds to the case where both the transmitter and receiver are PICO. The corrected amplitudes in Fig. 9(b) lie roughly within the curves, indicating that the effects of coupling and anelastic attenuation have been appropriately corrected. Similar results were obtained for all experiments.

4.2 CNN for estimating P -wave first motion polarity

To efficiently estimate many MTs, we adopted a CNN to automatically read the P -wave first motion polarities (Ross *et al.* 2018; Hara *et al.* 2019). For training a network, we prepared the data set as follows: From the DD-relocated events of all experiments, we extracted 3599 events for which $\text{SNR} \geq 15$ waveforms were obtained at 14 or more transducers. We manually read the P -wave first motion

polarities of the corresponding 86 376 waveforms. Thus, a total of 68 152 polarities were successfully read, including 51 333 polarities (up: 35 932; down: 15 401) for M304A and 16 819 (up: 12 259; down: 4560) for PICO. We used 80 per cent of the data set as the training data set and the remaining 20 per cent as the validation data set.

Fig. 10(a) shows our developed network, which used 150 sample waveforms around the theoretical arrival times as the input data. For each waveform $A(\tau)$, we applied z -score normalization

$$A_z(\tau) = \frac{A(\tau) - \mu}{\sigma}, \quad (7)$$

before inputting the waveforms to the network, where μ is the mean and σ is the standard deviation of $A(\tau)$. The network had 1-D convolutional layers (Kiranyaz *et al.* 2015) and fully connected layers. We used max-pooling (Krizhevsky *et al.* 2012) and global average pooling (Lin *et al.* 2013), which reduced the number of parameters, resulting in an efficient feature extraction and accuracy improvement. Dropout (Hinton *et al.* 2011) was used to suppress

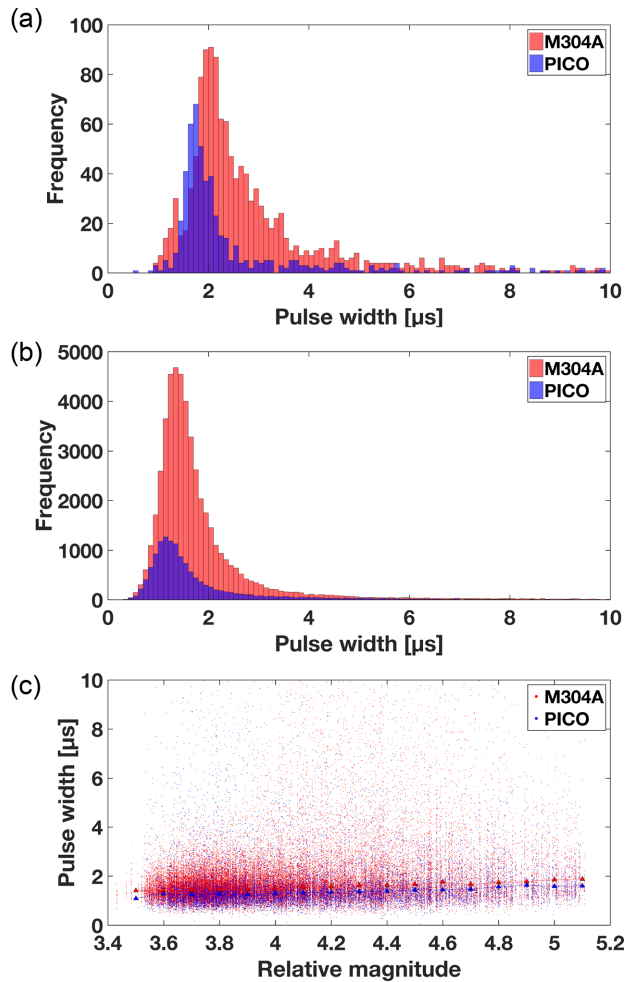


Figure 8. Histograms of the pulse widths of P -wave first motions obtained in (a) the pulse radiation tests and (b) hydraulic fracturing experiments (manual reading results). (c) Relation between relative magnitudes and pulse widths in the fracturing experiments, where the triangles show the median of the pulse widths for every 0.1-mag unit and the red and blue dots show the results obtained for M304A and PICO, respectively.

over-fitting. As activation functions, we applied sigmoid in the final layer and rectified linear unit (ReLU; Nair & Hinton 2010) in the others. In addition, binary cross-entropy was used as the loss function and Adam (Kingma & Ba 2014) as the optimizer. The prediction result obtained for the polarity of an input waveform was outputted as a continuous value between 0 and 1, where values close to 1 represent ‘up’ and 0 represent ‘down’.

Figs 10(b)–(e) depict changes in the loss and accuracy against the epochs (the number of times all input data are processed through a network) for the training and validation data sets. Here, we label the data ‘up’ (‘down’) when a prediction score is more (less) than 0.5, and calculate the accuracy based on this criterion. The two exactly same networks were trained separately for M304A and PICO. For the validation data set, the improvement in the loss and accuracy continued during the training for M304A but it stopped at epoch = 41 for PICO, indicating that over-fitting had started at that epoch. For polarity prediction, we used the parameters obtained at epoch = 100 for M304A and 41 for PICO. The accuracies for M304A and PICO at these epochs were 96.04 and 94.08 per cent, respectively. The use of a stricter criterion of 0.95 for up and 0.05 for down resulted in higher accuracies of 99.44 per cent for M304A and

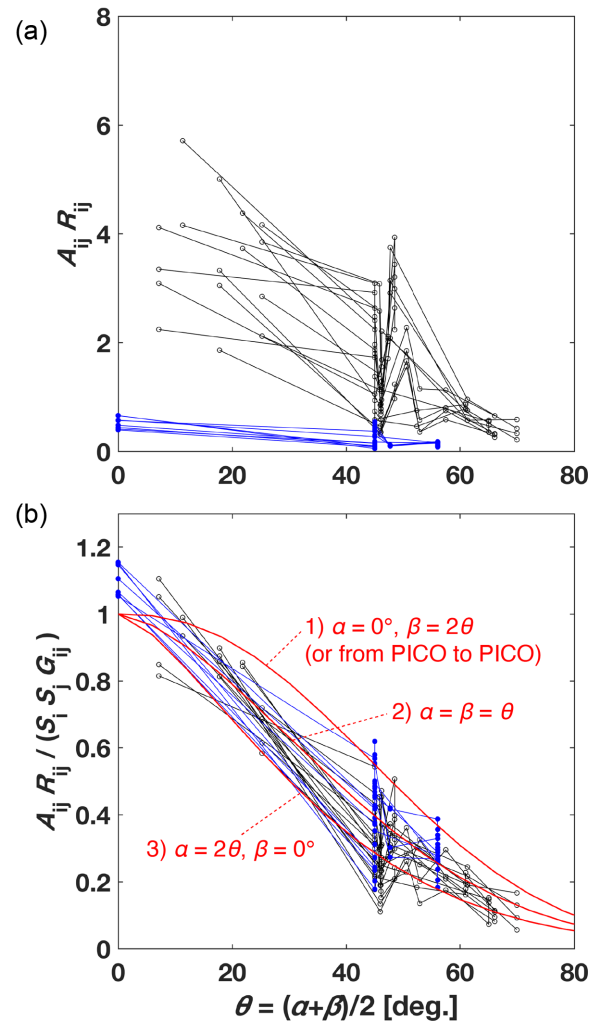


Figure 9. Results of the coupling coefficient and quality factor analysis conducted for KJG1810. (a) Raw amplitudes recorded at each receiver in the pulse radiation test. (b) Amplitudes corrected for the effects of coupling, geometrical spreading and anelastic attenuation. The horizontal axes denote the average θ of the incident angle α and projection angle β . The black and blue dots indicate the first motion amplitudes of waveforms received at M304A and PICO, respectively. Amplitudes recorded at the same receiver are connected by a line.

99.15 per cent for PICO. In the MT analysis, we used this criterion to select the prediction results.

4.3 Moment tensor inversion

Using the trained network, we read the P -wave first motion polarities for ~ 1.76 million waveforms of the DD-relocated events. The number of successful readings was 993 070 for M304A and 373 048 for PICO. To estimate the MTs, we also obtained the first motion amplitudes: the maximum (minimum) amplitudes of 30 samples around the theoretical arrival times for waveforms read as ‘up’ (‘down’).

Six independent components of MTs were estimated from the polarities and amplitudes of the events for which 10 or more polarities of M304A were obtained. We used the amplitudes after correcting the effects of sensor directivity, coupling condition, and attenuation. To correct the anelastic attenuation, we assumed $f = 385$ kHz,

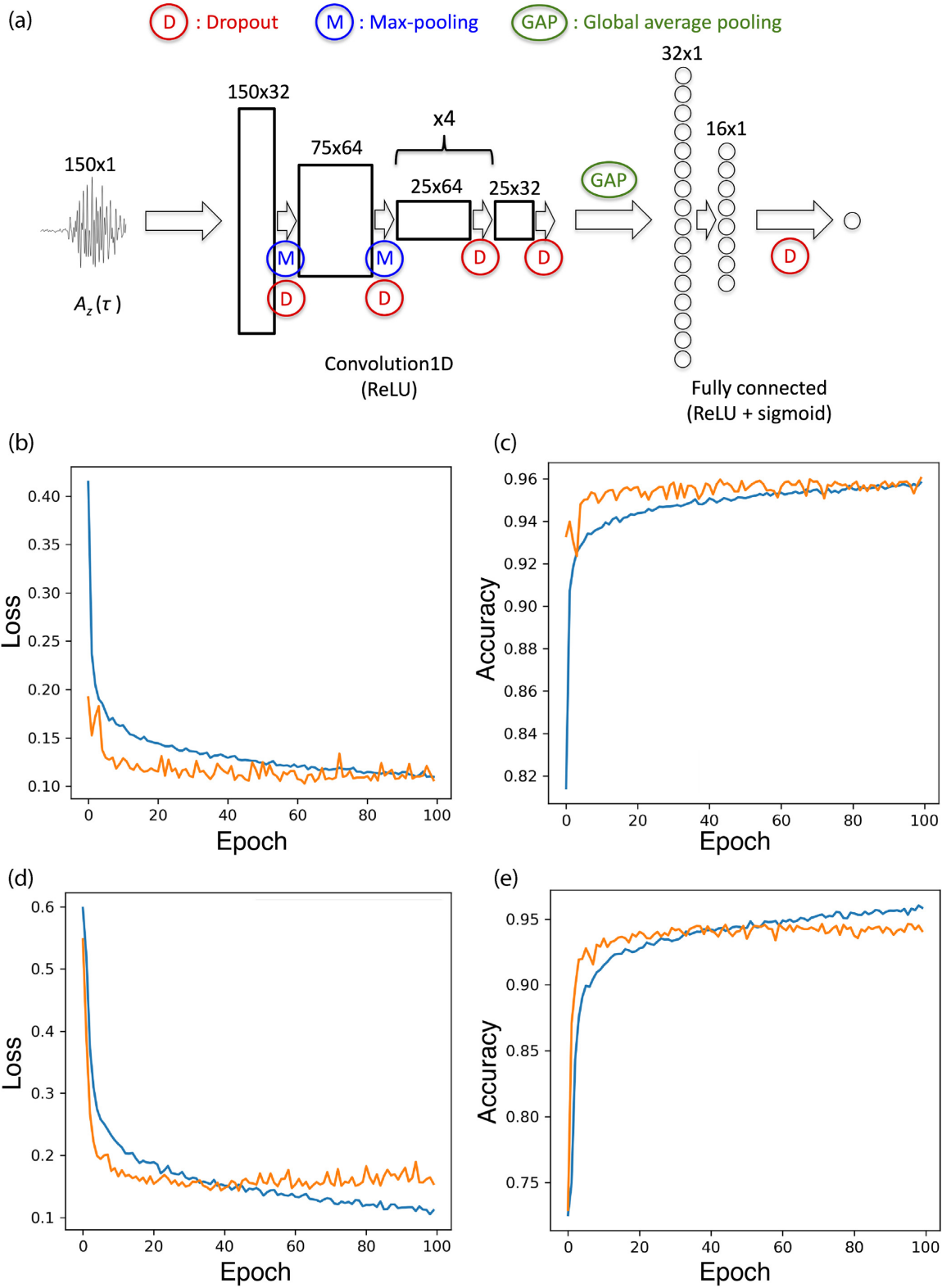


Figure 10. (a) CNN model for estimation of *P*-wave first motion polarity. Training results (changes in loss and accuracy) for waveforms received by (b and c) M304A and (d and e) PICO.

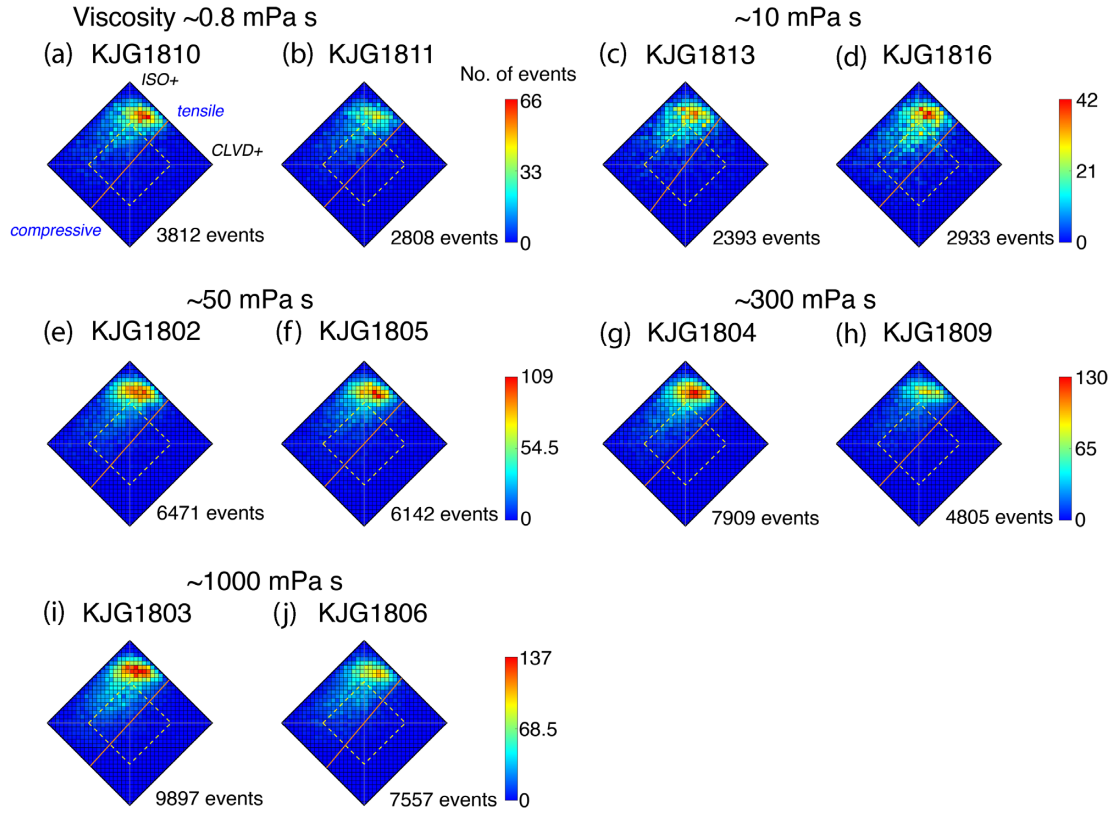


Figure 11. Source-type plots of MT solutions for each experiment. The colours indicate the number of events in each grid. Solutions in the dashed lines correspond to events with DC components of ≥ 50 per cent (i.e. $|c| \leq 0.5$). The orange line, which is evaluated from the ratio of V_P to V_S , corresponds to the ideal shear-tensile event (Vavryčuk, 2011, 2015). The right and left edges of the line correspond to pure tensile and compressive events, respectively.

which corresponded to the median of the pulse widths of the P -wave first motions of AE events during the fracturing experiments (Fig. 8b). This assumption is reasonable because the pulse widths did not depend on the relative magnitudes (Fig. 8c) but probably on the frequency responses of the AE transducers. The estimation method was the same as that used by Naoi *et al.* (2020), except that the effect of the anelastic attenuation was corrected.

For each MT, we calculated the variance reduction

$$R = \left(1 - \frac{\sum |A_e|^2}{\sum |A|^2}\right) \times 100, \quad (8)$$

to represent the consistency between the theoretical and observed amplitudes, where A indicates the observed amplitude of the P -wave first motions for individual sensors and A_e indicates the residuals of the amplitudes for the inversion results. In the following analysis, we used MT solutions with $R \geq 50$.

We decomposed the MTs into isotropic (ISO), shear (double couple; DC) and compensated linear vector dipole (CLVD) components by using the simplified decomposition method (Vavryčuk 2015). We calculated the consistency coefficient c (Vavryčuk 2011) as follows:

$$c = \text{sign} \left(\frac{M_{\text{ISO}}}{M_{\text{CLVD}}} \right) \left| 1 - \frac{M_{\text{DC}}}{100} \right|, \quad (9)$$

where M_{ISO} , M_{CLVD} and M_{DC} indicate the percentage of each component. The variable c takes a value between -1 and 1 , and MTs with $c \geq 0$ correspond to a shear-tensile model where shear and opening (closure) occur in a single-crack surface (Vavryčuk 2011). A c value close to 1 indicates the dominance of a tensile (corresponding to crack opening) or compressive (crack closure) component, while a

value close to 0 indicates the dominance of a shear component. In addition, we calculated the fault-normal vector \mathbf{n} and dislocation vector \mathbf{v} using the following equations (Vavryčuk 2011):

$$\mathbf{n} = \sqrt{\frac{M_1 - M_2}{M_1 - M_3}} \mathbf{e}_1 + \sqrt{\frac{M_3 - M_2}{M_3 - M_1}} \mathbf{e}_3, \quad (10)$$

$$\mathbf{v} = \sqrt{\frac{M_1 - M_2}{M_1 - M_3}} \mathbf{e}_1 - \sqrt{\frac{M_3 - M_2}{M_3 - M_1}} \mathbf{e}_3, \quad (11)$$

where M_1 , M_2 and M_3 indicate the maximum, intermediate, and minimum eigenvalues of MTs, respectively, and \mathbf{e}_1 , \mathbf{e}_2 and \mathbf{e}_3 indicate the corresponding eigenvectors. \mathbf{n} and \mathbf{v} have complementary solutions, where eq. (10) yields the dislocation vector, and eq. (11) yields the fault-normal vector.

Fig. 11 shows the source-type plots of the MTs for each experiment, where the use of CNN allowed us to estimate a large number of (54 727) solutions. In all plots, events were concentrated in the upper right regions, indicating that tensile events were dominant regardless of the fracturing fluid viscosity. Hubbert & Willis (1957) expected that hydraulic fractures would have a tensile mechanism opening along the direction of the minimum principal stress. To confirm whether the obtained MTs corresponded to the expected mechanism, we observed the directions of the vectors \mathbf{n} and \mathbf{v} ; that is, we calculated φ , the smaller one of the angles between these vectors and the y -direction (i.e. the theoretical opening direction). The results are shown in Fig. 12, which shows only the events that satisfy $c > 0.5$ and $M_{\text{ISO}} \geq 0$ (tensile-dominated events). Regardless of the viscosity, events with various opening axes occurred before t^{init} . In the second expansion phase, events with orientations close

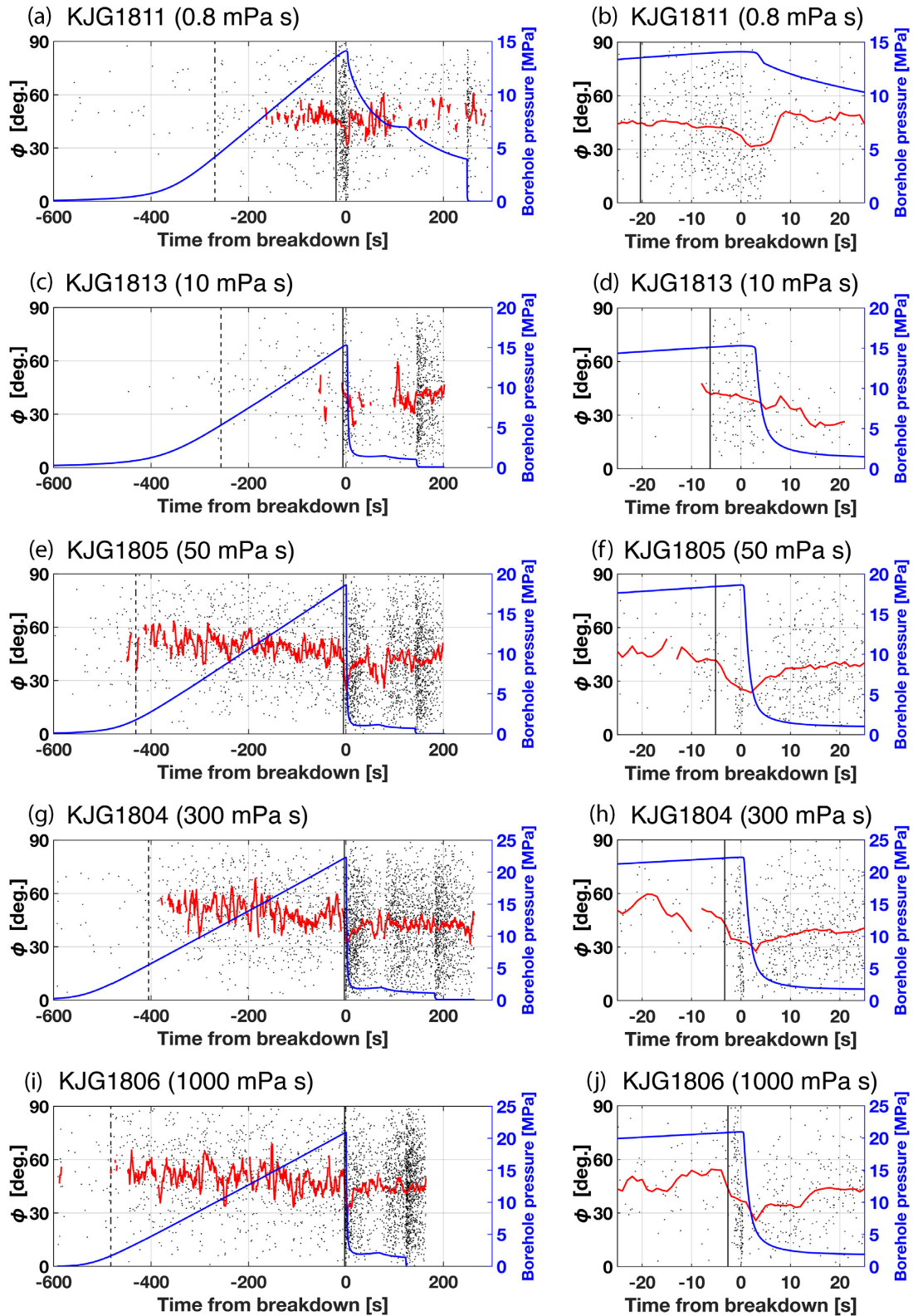


Figure 12. (a, c, e, g and i) Temporal changes in ϕ , which is the smaller angle between the y -axis and the two candidates of crack-opening axes of each MT solution. The black dots indicate the angles for the solutions satisfying $c > 0.5$ and $M_{ISO} \geq 0$ (i.e. tensile-dominated events). The red lines indicate the moving average of ϕ in each 6-s window (the results only for windows containing five or more events are plotted). The blue lines indicate the borehole pressure history. The dashed black lines indicate the time at which the AE occurrence rate exceeds four events s^{-1} . The solid black lines indicate t^{init} . (b, d, f, h and j) Enlarged views of (a), (c), (e), (g) and (i), respectively, around t^{BD} .

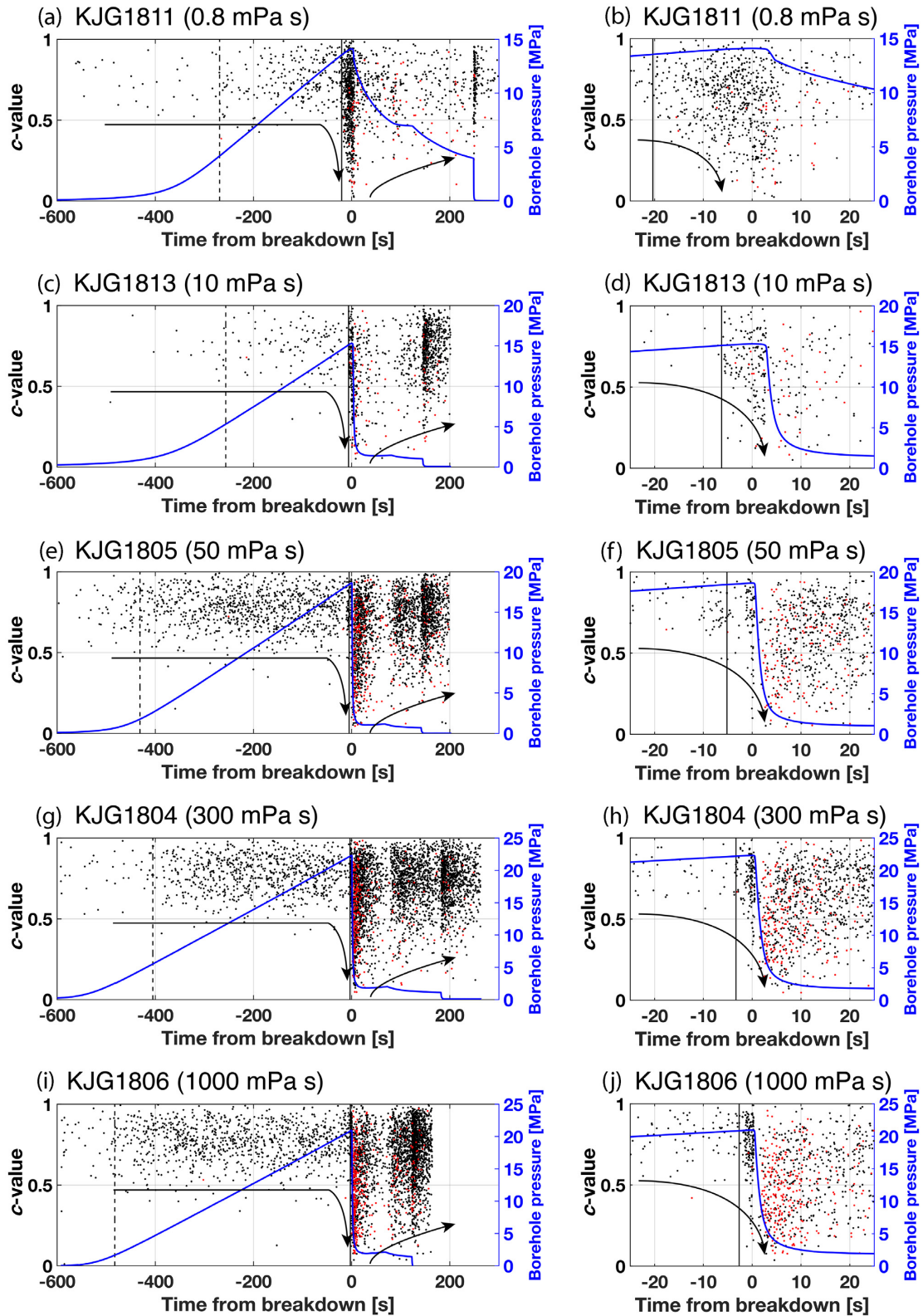


Figure 13. (a, c, e, g and i) Temporal changes in the c -values for the obtained MT solutions (only $c \geq 0$). The black and red dots indicate the solutions with $M_{150} \geq 0$ and $M_{150} < 0$, respectively. The blue lines indicate borehole pressure history. The black lines indicate the time at which the AE occurrence rate exceeds four events in 1 s. The solid black lines show t^{mit} . (b, d, f, h and j) Enlarged views of (a), (c), (e), (g) and (i) around t^{BD} .

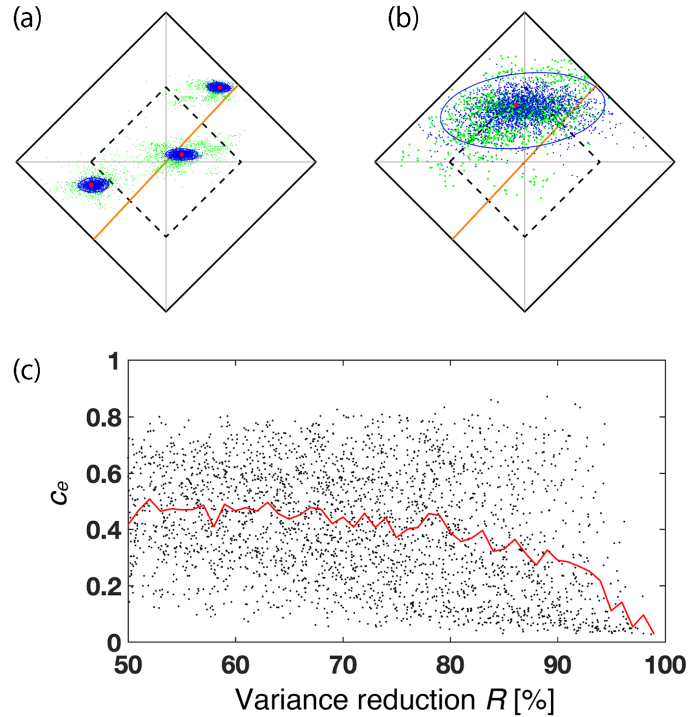


Figure 14. Uncertainty of MT solutions obtained for KJG1811 experiment. (a) Examples of reliable solutions ($c_e = 0.03\text{--}0.05$ and $R = 88.7\text{--}97.5$). (b) An example of unreliable solutions ($c_e = 0.51$ and $R = 62.3$). The blue and green dots indicate bootstrap and jackknife results, respectively. The blue ellipses represent 95 per cent confidence regions estimated from the bootstrap results, and the red dots indicate the best solutions. (c) Relation between R and c_e obtained by the bootstrap approach for all MT solutions. The red line shows the average of c_e for every 1.0-interval bin of R .

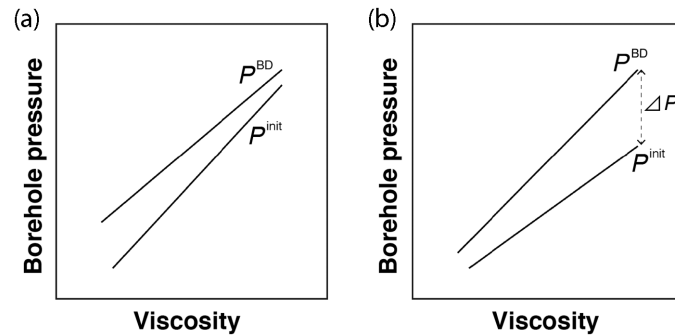


Figure 15. Relationship of fracturing fluid viscosity to P^{BD} and P^{init} . (a) The case where $\Delta P = P^{BD} - P^{init}$ decreases with increasing viscosity (this study). (b) The case where ΔP increases with increasing viscosity (Zoback & Pollard 1978; Shimizu *et al.* 2011; Stanchits *et al.* 2015).

to the theoretically expected direction ($\varphi = 0$) frequently occurred, which rarely occurred before t^{init} . After breakdown, the fraction of such events decreased.

To observe temporal changes in the focal mechanisms, we estimated the temporal variation in c for $c \geq 0$, where the events were consistent with the shear–tensile model (Fig. 13). Regardless of the viscosity, events with a larger tensile component (events with larger c and positive M_{ISO}) dominantly occurred before t^{init} . From t^{init} , events with smaller c increased with time. Until 5–15 s after t^{BD} , events with c ranging from 0 to 1, including shear-dominated events, occurred. Thereafter, events with a larger c dominated again. Compressive-dominated events (events with larger c and negative M_{ISO}) began to occur after t^{init} and more frequently after t^{BD} .

To investigate the reliability of the above findings, we evaluated the uncertainties of MT solutions using the residual bootstrap approach (e.g. Ford *et al.* 2009). Figs 14(a) and (b) show examples of

source-type plots for solutions obtained from 2000 bootstrap samples with 95 per cent confidence ellipses calculated from the results. We also tested the jackknife approach (e.g. Boyd *et al.* 2015) by removing 1, 2 and 3 sensors in the inversion process. In Figs 14(a) and (b), the jackknife solutions were plotted after the correction with the scale factor of $\sqrt{(n-j-5)}/\sqrt{j}$ (e.g. Tichelaar & Ruff 1989), where n and j are the number of sensors used in the inversion, and removed sensors (i.e. 1–3), respectively, for the deviation from the best solution (the solution without the removal) in each of the six independent MT components. As shown in the figure, the results are roughly similar to the bootstrap ones, and hence we discuss only the former results in the following. Fig. 14a (b) shows examples of reliable (unreliable) solutions with small (large) uncertainties.

As shown in Fig. 14(b), MT solutions with large errors were used in Figs 11–13, but the tendencies observed in many solutions in the above discussion are likely to be reliable. Here, we introduce the

standard error of c -values (c_e) estimated by the bootstrap approach to select reliable solutions. Fig. 14(c) shows the relationship between R and c_e for every solution of KJG1811. As shown in Fig. 14(c), c_e is significantly small for $R > 80$, but there are also many solutions with small c_e for small R values. In Supporting Information Figs S1–S3, only the solutions satisfying $c_e < 0.2$ are plotted in the same format as Figs 11–13. We can find tendencies similar to those discussed above, although the temporal resolutions are low.

5 DISCUSSION

5.1 Two preparatory phases of hydraulic fracture formation

In the present study, we identified two preparatory phases of AE activity prior to the breakdown, whose active regions expanded outward from the pressurized section of the borehole. The first expansion phase began when the borehole pressure was several MPa, typically 10–30 per cent of the breakdown pressure. During this phase, the AE-active region expanded three-dimensionally from the pressurized section to the outside. The activity comprised tensile-dominated events with various opening axes, which were likely to be attributed to the penetration of the fracturing fluid into pre-existing microcracks, such as grain boundaries. The second expansion phase began simultaneously with the deviation of the borehole pressure from its linearly increasing trend, which occurred at 90–99 per cent of the breakdown pressure. During this phase, another AE-active region expanded two-dimensionally from the pressurized section along the maximum compression axis. In addition, tensile-dominated events with opening axes close to the y -direction, which were rare in the first expansion phase, occurred frequently. These features are consistent with the classical theory of hydraulic fracturing, and we consider that the second expansion phase corresponds to the formation of a main hydraulic fracture. In this phase, many shear-dominated events also occurred, which were rarely observed in the first expansion phase. After the breakdown, the fraction of shear-dominated events decreased and tensile-dominated events became dominant again. Meanwhile, compression-dominated events also occurred, possibly due to the decrease in the fluid pressure inside the induced fractures.

The average relative magnitudes in the second expansion phase increased compared to those in the first expansion phase. We interpreted that the AE magnitudes in the first expansion phase bear a relationship with the scale of the pre-existing microcracks (grain boundaries). Meanwhile, the magnitudes in the second expansion phase were likely to have been constrained by larger stress concentrations because of the higher borehole pressure and the presence of induced fractures, generating larger AEs. While the existence of the second expansion phase has been confirmed previously (Stanchits *et al.* 2015; Naoi *et al.* 2018; Yamamoto *et al.* 2019), the first expansion phase was discovered for the first time in the present study. The use of high-sensitivity AE sensors with a built-in pre-amplifier enabled us to detect very small AEs in the first expansion phase.

Shear events have been predominantly detected in actual production fields (e.g. Maxwell & Cipolla 2011; Šílený *et al.* 2014). Some previous studies suggested that shear events induced by hydraulic fracturing had larger magnitudes than tensile events, resulting in the dominance of detected shear events (Ishida *et al.* 2004; Shimizu *et al.* 2011; Maxwell & Cipolla 2011). In this study, the averages of relative magnitudes were greater for shear-dominated events, reflecting the fact that they occurred intensively in the latter half of

the second expansion phase, where the fraction of large events was greater. Meanwhile, as shown in Figs 3(f) and 5(f), many of the tensile-dominated events ($c \sim 1$) were as large as the largest shear-dominated events ($c \sim 0$), which do not support the expectation of the previous studies.

Apparently, the AE activity during hydraulic fracturing strongly depends on the rock type. Naoi *et al.* (2020) conducted hydraulic fracturing experiments in a laboratory on a very tight Eagle Ford shale under the same setting as that used in the present study. They likely detected AEs as small as those in the present experiments. However, only one simple AE activity that delineated a growing main fracture was observed: it occurred during ~ 10 s preceding the breakdown and exhibited focal mechanisms of tensile cracks, as expected from the classical theory of hydraulic fracturing. Unlike the previous study, in the present study, we observed various AE activities, such as the activity caused by fluid penetration in the first expansion phase, many shear-dominated events in the second expansion phase, and activity after the breakdown. Such differences are attributable to the presence of pre-existing microcracks (grain boundaries) of Kurokami-jima granite. The hydraulically induced AE activity in the granite was presumably affected by fluid penetration into pre-existing microcracks and their interaction with the induced fractures. The importance of interactions among discrete fractures has been indicated in the generation process of shear fractures in rock compression tests (Reches & Lockner 1994) and magma-induced seismic swarming (Hill 1977).

5.2 Viscosity dependence of borehole pressure

In this study, the breakdown pressure, P^{BD} , and fracture initiation pressure, P^{init} , increased with the viscosity of the fracturing fluid. Similar trends have been repeatedly confirmed through laboratory experiments (Zoback & Pollard 1978; Stanchits *et al.* 2015; Ishida *et al.* 2016; Fallahzadeh *et al.* 2017) and numerical simulations (Shimizu *et al.* 2011). It has been proposed that the viscosity dependence of the borehole pressure is caused by the difference in pore pressure induced by the penetration of the fracturing fluid into the rock matrix around a borehole. In other words, an increase in the pore pressure decreases the effective stress, decreasing the borehole pressure required for the formation of the main tensile fracture (Hubbert & Willis 1957). The penetration of a higher-viscosity fluid into a rock matrix is more difficult, resulting in a decrease in the pore pressure around the borehole and an increase in the borehole pressure required for fracturing (Zoback & Pollard 1978; Shimizu *et al.* 2011). The previous studies also proposed a mechanism whereby the penetration of a higher-viscosity fluid into an induced fracture is more difficult, which suppresses an increase in the stress intensity factor at the fracture tip. These mechanisms are likely to have caused the viscosity dependence of P^{BD} and P^{init} observed in this study.

In the present experiments, the increase rates of P^{init} against viscosity were greater than those of P^{BD} (Fig. 6b), and hence, $\Delta P = P^{BD} - P^{init}$ decreased with increasing viscosity, as shown in Fig. 15(a). Meanwhile, the opposite trend, as shown in Fig. 15(b), has been observed in some previous studies on hydraulic fracturing conducted in a laboratory (Zoback & Pollard 1978; Stanchits *et al.* 2015) and through numerical simulation (Shimizu *et al.* 2011). As the two aforementioned mechanisms indicate that the use of high-viscosity fluid suppresses crack propagation, they cause an increase in ΔP with viscosity, as shown in Fig. 15(b); hence, another mechanism is required to explain the currently observed ΔP trend.

One possibility for this is that the fluid pressure is transferred to a crack tip with a small pressure loss, even when a high-viscosity fluid is used. If the increase rate of P^{init} against viscosity exceeds that of the pressure loss in a fracture, the stress intensity factor and crack propagation speed can increase with viscosity. The stress intensity factor after fracture initiation is likely to be determined by the balance between the initiation pressure and pressure loss that occurred in the induced fractures, pre-existing microcracks, and pores. The condition for the ΔP trend can possibly be investigated with numerical simulation, such as that performed by Shimizu *et al.* (2011).

6 CONCLUSIONS

To investigate the effect of the viscosity of the fracturing fluid on hydraulic fracturing, we conducted hydraulic fracturing experiments on Kurokami-jima granite in a laboratory, using fracturing fluids with multiple viscosities. We performed AE measurements with high-performance sensors and direct observation of fluid penetration regions using the fluorescent method. In addition, to observe temporal changes in the focal mechanisms, we estimated many (54 727) MTs by introducing a deep learning technique. Based on these observations and analysis, we found two preparatory phases preceding the breakdown. The first expansion phase corresponded to fluid penetration into the rock matrix, accompanied by small tensile AEs in various orientations that expanded three-dimensionally, and the second expansion phase corresponded to the initiation and propagation of a main hydraulic fracture, which was delineated by a two-dimensional AE distribution. In the second phase, the duration and initiation pressure clearly depended on the viscosity of the fracturing fluid, and a significant number of shear events occurred. Such complicated preparatory phases and their dependence on the fracturing fluid's viscosity were likely to have been caused by the interactions among the fracturing fluid, pre-existing microcracks, and induced fractures. The results of this study would, therefore, be useful for understanding the hydraulic fracture behaviour in not only granite but also the rock mass containing many pre-existing fractures.

ACKNOWLEDGEMENTS

This study was financially supported by the Japan Oil, Gas and Metals National Corporation (JOGMEC), JSPS KAKENHI Grant Number 16H04614, and the Kyoto University Foundation. The data used in the manuscript are not open to the public.

REFERENCES

- Akai, T., Yano, S., Kurosawa, I., Chen, Y. & Ishida, T., 2015. Consideration on shape of hydraulic fracture based on laboratory experiment, in *Abu Dhabi International Petroleum Exhibition and Conference*, 9–12 November, Abu Dhabi, UAE, SPE-177673-MS, doi:10.2118/177673-MS.
- Aker, E., Kühn, D., Vavříček, V., Soldal, M. & Oye, V., 2014. Experimental investigation of acoustic emissions and their moment tensors in rock during failure, *Int. J. Rock Mech. Min. Sci.*, **70**, 286–295.
- Allen, R.V., 1978. Automatic earthquake recognition and timing from single traces, *Bull. seism. Soc. Am.*, **68**, 1521–1532.
- Boyd, O.S., Dreger, D.S., Lai, V.H. & Gritto, R., 2015. A systematic analysis of seismic moment tensor at the geysers geothermal field, California, *Bull. seism. Soc. Am.*, **105**, 2969–2986.
- Chen, Y., Nagaya, Y. & Ishida, T., 2015. Observations of fractures induced by hydraulic fracturing in anisotropic granite, *Rock Mech. Rock Eng.*, **48**, 1455–1461.
- Chen, Y., Naoi, M., Tomonaga, Y., Akai, T., Tanaka, H., Takagi, S. & Ishida, T., 2018. Method for visualizing fractures induced by laboratory-based hydraulic fracturing and its application to shale samples, *Energies*, **11**, 1976, doi:10.3390/en11081976.
- Fallahzadeh, S.H., Hossain, M.M., Cornwell, A.J. & Rasouli, V., 2017. Near wellbore hydraulic fracture propagation from perforations in tight rocks: the roles of fracturing fluid viscosity and injection rate, *Energies*, **10**, 359, doi:10.3390/en10030359.
- Ford, S.R., Dreger, D.S. & Walter, W.R., 2009. Identifying isotropic events using a regional moment tensor inversion, *J. geophys. Res.*, **114**, B01306, doi:10.1029/2008JB005743.
- Hara, S., Fukahata, Y. & Iio, Y., 2019. P-wave first-motion polarity determination of waveform data in western Japan using deep learning, *Earth Planets Space*, **71**, 127, doi:10.1186/s40623-019-1111-x.
- Hill, D.P., 1977. A model for earthquake swarms, *J. geophys. Res.*, **82**, 1347–1352.
- Hinton, G.E., Srivastava, N., Krizhevsky, A., Sutskever, I. & Salakhutdinov, R.R., 2011. Improving neural networks by preventing co-adaptation of feature detectors, (arXiv:1207.0580).
- Hubbert, M.K. & Willis, D.G., 1957. Mechanics of hydraulic fracturing, *Trans. Soc. Pet. Eng. AIME*, **210**, 153–168.
- Ishida, T., Chen, Q., Mizuta, Y. & Roegiers, J.C., 2004. Influence of fluid viscosity on the hydraulic fracturing mechanism, *J. Energy Resour. Technol.*, **126**, 190–200.
- Ishida, T. *et al.*, 2016. Features of CO₂ fracturing deduced from acoustic emission and microscopy in laboratory experiments, *J. geophys. Res.*, **121**, 11, 8080–8098.
- Kudo, Y., Hashimoto, K., Sano, O. & Nagasawa, K., 1986. The empirical knowledge of quarryman and physical properties of granite, *Soil Mech. Found. Eng.*, **34**, 47–51 (in Japanese).
- Kudo, Y., Hashimoto, K., Sano, O. & Nagasawa, K., 1987. Anisotropy of granite rock in the inland sea in western Japan, *J. Jpn. Soc. Civil Eng.*, **382**, 45–53 (in Japanese).
- Kingma, D.P. & Ba, J., 2014. Adam: a method for stochastic optimization, in *3rd International Conference for Learning Representations*, San Diego.
- Kiranyaz, S., Ince, T., Hamila, R. & Gabbouj, M., 2015. Convolutional neural networks for patient-specific ECG classification, in *IEEE-EMBS, Milan*, pp. 2608–2611, doi:10.1109/EMBC.2015.7318926.
- Krizhevsky, A., Sutskever, I. & Hinton, G.E., 2012. ImageNet classification with deep convolutional neural networks, *NeurIPS*, **25**, 1097–1105.
- Kwiatk, G., Charalampidou, E.M., Dresen, G. & Stanchits, S., 2014. An improved method for seismic moment tensor inversion of acoustic emissions through assessment of sensor coupling and sensitivity to incidence angle, *Int. J. Rock Mech. Min. Sci.*, **65**, 153–161.
- LeCun, Y., Botton, L., Bengio, P. & Haffner, P., 1998. Gradient-based learning applied to document recognition, *Proc. IEEE*, **86**, 2278–2324.
- Lin, M., Chen, Q. & Yan, S., 2013. Network in Network, preprint (arXiv:1312.4400).
- Mayerhofer, J., Lolon, P., Warpinski, R., Cipolla, L., Walser, D. & Rightmire, M., 2010. What is stimulated reservoir volume? *SPE Prod. Oper.*, SPE-119890-PA, doi:10.2118/119890-PA.
- Maxwell, S.C. & Cipolla, C., 2011. What does microseismicity tell us about hydraulic fracturing?, *Soc. Pet. Eng. ATCE*, Denver, CO, SPE146932, doi:487 10.2118/146932-MS.
- Nair, V. & Hinton, G.E., 2010. Rectified linear units improve restricted Boltzmann machines, in *Proceedings of the 27th International Conference on Machine Learning*, Haifa, Israel, pp. 807–814.
- Nara, Y. & Kaneko, K., 2006. Sub-critical crack growth in anisotropic rock, *Int. J. Rock Mech. Min. Sci.*, **43**, 437–453.
- Naoi, M. *et al.*, 2018. Monitoring hydraulically-induced fractures in the laboratory using acoustic emissions and the fluorescent method, *Int. J. Rock Mech. Min. Sci.*, **104**, 53–63.
- Naoi, M. *et al.*, 2020. Tensile-dominant fractures observed in hydraulic fracturing laboratory experiment using Eagle Ford shale, *Geophys. J. Int.*, **222**, 769–780.
- Reches, Z. & Lockner, D.A., 1994. Nucleation and growth of faults in brittle rocks, *J. geophys. Res.*, **99**, 18 159–18 173.

- Ross, Z.E., Meier, M.A. & Hauksson, E., 2018. *P* wave arrival picking and first-motion polarity determination with deep learning, *J. geophys. Res.*, **123**, 5120–5129.
- Rothman, R.L., Greenfield, R.J. & Hardy, H.R., 1974. Errors in hypocenter location due to velocity anisotropy, *Bull. seism. Soc. Am.*, **64**, 1993–1996.
- Sano, O., Kudo, Y. & Mizuta, Y., 1992. Experimental determination of elastic constants of Oshima granite, Barre granite, and Chelmsford granite, *J. geophys. Res.*, **97**, 3367–3379.
- Shimizu, H., Murata, S. & Ishida, T., 2011. The distinct element analysis for hydraulic fracturing in hard rock considering fluid viscosity and particle size distribution, *Int. J. Rock Mech. Min. Sci.*, **48**, 712–727.
- Šílený, J., Jechumtálová, Z. & Dorbath, C., 2014. Small scale earthquake mechanisms induced by fluid injection at the enhanced geothermal system reservoir Soultz (Alsace) in 2003 using alternative source models, *Pure appl. Geophys.*, **171**, 2783–2804.
- Stanchits, S., Surdi, A., Gathogo, P., Edelman, E. & Suarez-Rivera, R., 2014. Onset of hydraulic fracture initiation monitored by acoustic emission and volumetric deformation measurements, *Rock Mech. Rock Eng.*, **47**, 1521–1532.
- Stanchits, S., Burghardt, J. & Surdi, A., 2015. Hydraulic fracturing of heterogeneous rock monitored by acoustic emission, *Rock Mech. Rock Eng.*, **48**, 2513–2527.
- Stierle, E., Vavryčuk, V., Kwiątek, G., Charalampidou, E.M. & Bohnhoff, M., 2016. Seismic moment tensors of acoustic emissions recorded during laboratory rock deformation experiments: sensitivity to attenuation and anisotropy, *Geophys. J. Int.*, **205**, 38–50.
- Takanami, T. & Kitagawa, G., 1988. A new efficient procedure for the estimation of onset times of seismic waves, *J. Phys. Earth*, **36**, 267–290.
- Tichelaar, B.W. & Ruff, L.J., 1989. How good are our best models? Jackknifing, bootstrapping, and earthquake depth, *EOS, Trans. Am. geophys. Un.*, **70**, 593–606.
- Vavryčuk, V., 2011. Tensile earthquakes: theory, modeling and inversion, *J. geophys. Res.*, **116**, doi: 10.1029/2011JB008770.
- Vavryčuk, V., 2015. Moment tensor decompositions revisited, *J. Seismol.*, **19**, 231–252.
- Waldhauser, F. & Ellsworth, W.L., 2000. A double-difference earthquake location algorithm: method and application to the northern Hayward fault, California, *Bull. seism. Soc. Am.*, **90**, 1353–1368.
- Warpinski, N.R., Kramm, R.C., Heinze, J.R. & Waltman, C.K., 2005. Comparison of single- and dual-array microseismic mapping techniques in the Barnett shale, *SPE Annual Technical Conference and Exhibition*, SPE-95568-MS.
- Yamamoto, K. et al., 2019. Moment tensor analysis of acoustic emissions induced by laboratory-based hydraulic fracturing in granite, *Geophys. J. Int.*, **216**, 1507–1516.
- Zhang, B., Li, X., Zhang, Z., Wu, Y., Wu, Y. & Wang, Y., 2016. Numerical investigation of influence of *in-situ* stress ratio, injection rate and fluid viscosity on hydraulic fracture propagation using a distinct element approach, *Energies*, **9**, 140, doi:10.3390/en9030140.
- Zoback, M.D. & Pollard, D.D., 1978. Hydraulic fracture propagation and the interpretation of pressure-time records for *in-situ* stress determinations, *Proceedings of 19th US Rock Mech. Symp.*, Mackay School of Mines, Reno, Nevada, 14–22.

SUPPORTING INFORMATION

Supplementary data are available at *GJI* online.

Figure S1. Source-type plots of MT solutions for each experiment. The format is the same as Fig. 11.

Figure S2. Temporal changes in φ , which is the smaller angle between the *y*-axis and the two candidates of the crack-opening axes of each MT solution. The format is the same as Fig. 12.

Figure S3. Temporal changes in the *c*-values for the obtained MT solutions (only $c \geq 0$). The format is the same as Fig. 13.

Please note: Oxford University Press is not responsible for the content or functionality of any supporting materials supplied by the authors. Any queries (other than missing material) should be directed to the corresponding author for the paper.